第 31 卷第 4 期
2015 年 4 月

无 机 化 学 学 报
CHINESE JOURNAL OF INORGANIC CHEMISTRY

Vol.31 No.4
649-658

硫掺杂氧化锡纳米材料的固相合成及其可见光降解百草枯

贺仲兵[1,2] 刘少友*[,1,3] 闵宗义[2] 杨红芸[1] 聂 信[1]

([1]凯里学院化学与材料工程学院,凯里 556011)

([2]湖南大学环境科学与工程学院,长沙 432001)

([3]广西大学环境学院,南宁 530004)

摘要:以十二烷基苯磺酸钠(SDBS)为模板,采用低温固相反应法合成了硫掺杂二氧化锡(S-SnO_2)纳米粉体材料,并用 XRD、XPS、SEM、UV-Vis、FTIR 及 HR-TEM 等技术对材料进行了表征,探讨了 S 掺杂 SnO_2 纳米材料对百草枯的可见光降解性能,分析了 S 掺杂效应的作用机理。结果表明,采用固相反应法所得 SnO_2 及 S-SnO_2 纳米材料的禁带宽度变窄,SDBS 对材料的表面结构具有一定的调控作用。S 是以 S(Ⅳ)和 S(Ⅵ)的形式进入 SnO_2 晶格形成 $Sn_{1-x}S_xO_2$ 晶体结构而不是进入 SnO_2 晶格间隙,Sn-O-S 键的弯曲振动峰介于 930~980 cm^{-1} 之间。S 的掺杂使 SnO_2 纳米材料表面活性增强,光催化降解百草枯的活性依次为 SnO_2<$SnO_{2(SDBS)}$<S-SnO_2<S-$SnO_{2(SDBS)}$,2 h 内,S-$SnO_{2(SDBS)}$样品对除草剂百草枯的光催化活性达 95.2%,其主要原因是 S-$SnO_{2(SDBS)}$材料表面有更多的羟基和进入 SnO_2 晶格的 S,有利光生电荷的有效分离。

关键词:硫掺杂;二氧化锡;固相合成;可见光降解;百草枯

中图分类号:O643.36 **文献标识码**:A **文章编号**:1001-4861(2015)04-0649-10

DOI:10.11862/CJIC.2015.117

Sulfur Doped Tin Oxide Nanoparticles: Solid State Synthesis and Performance for Visible-Light Driven Photocatalytic Degradation of Paraquat

HE Zhong-Bing[1,2] LIU Shao-You*[,1,3] YANG Hong-Yun[1] MIN Zong-Yi[2] NIE Xin[1]

([1]*College of Chemistry and Materials Engineering, Kaili University, Kaili, Guizhou* 556011, *China*)

([2]*College of Envirnomental Science and Engineering, Hunan University, Changsha* 410082, *China*)

([3]*School of Envirnomental Studies, Guangxi University, Nanning* 530004, *China*)

Abstract: Sulfur doped tin oxide (S-SnO_2) nanoparticles with high visible light-driven activity was synthesized by a facile solid state synthesis approach at low temperature using sodium dodecyl benzene sulfonate (SDBS) as a template. The samples were characterized by XRD, XPS, SEM, UV-Vis, HR-TEM, and FTIR. The doping mechanism and photocatalytic degradation of paraquat under visible light irradiation were investigated. The results show that the SDBS has a significant regulating effect on the surficial structure for both SnO_2 and S-SnO_2 prepared by solid state synthesis. The S element is successfully incorporated into the lattice of SnO_2 with S(Ⅳ) and S(Ⅵ) rather than embeds into the interstice of SnO_2 lattice. S-doping enhances the photocatalytic activity of SnO_2 due to the presence of a large number of hydroxyls on the surface and S(Ⅵ) in the lattice of SnO_2 benefiting the light absorption and effective charge separation, and it follows an order of SnO_2<S-SnO_2<$SnO_{2(SDBS)}$<S-$SnO_{2(SDBS)}$.

Key words: S-doped; SnO_2; solid state synthesis; photocatalytic degradation; paraquat

收稿日期:2014-09-01。收修改稿日期:2015-02-08。

贵州省科技创新人才团队建设基金项目(黔科人字[2013]4029);贵州省材料物理与化学特色重点学科建设基金项目(黔教高发[2011]208);贵州省教育厅特色重点实验室建设基金项目(黔教高发[2012]196);贵州省教育厅市州地普通本科高校教育质量提升科研项目(黔教高发[2011]278-01)资助。

*通讯联系人。E-mail:lsy651204@163.com

0 Introduction

Paraquat (1,1′-Dimethyl-4,4′-bipyridinium) is a quick-acting and non-selective contact herbicide, and it could kill green plant tissue on contact[1]. It is highly toxic to human beings and animals, potentially leading to acute respiratory distress syndrome (ARDS), and there are no specific antidotes[2]. It is also reported that paraquat may be considered as persistent organic pollutants as it could persist in soil for a long time (with a half-life up to 20 years) and accumulate in various organisms through the food chain, which can lead to various health problems to human beings, including teratogenicity, carcinogenicity and mutagenicity[3]. Furthermore, paraquat could be rapidly adsorbed and strongly bonded to clay and organic matter in the soil, and it shows biologically inert and cannot be taken up by plant roots or other organisms[4]. Thus, the extensive use of paraquat leads to severe contamination of soil and groundwater, which may pose adverse effects on the environmental ecosystem and human health. Therefore, it is of practical importance to find out an effective way to remove paraquat from polluted waters.

SnO_2, usually comprised of tetragonal, hexagonal and orthorhombic crystal systems, has been widely used in gas sensor, semiconductor, spectralite and transparency electrode because of its low resistivity and high transmittance[5]. SnO_2 as a n-type semiconductor with wide band gap (3.8 eV) is an excellent photocatalyst[6-8]. However, due to its wide band gap, SnO_2 photocatalysis could only utilize UV light with $\lambda<330$ nm, which is less than about 3% of the sunlight spectrum, limiting its application by directly and fully utilizing the solar energy. Hence, great efforts have been made to enhance the visible light photocatalytic activity of SnO_2, such as doping with metal/nonmetal elements to change the energy level and consequently broadening light responsive range to visible light region[9-12].

Sulfur is a multivalent element, and different doping technologies lead to different chemical states of sulfur in the crystal lattice and subsequently to exhibit different photocatalytic activities[13-14]. As a facile, efficient and promising preparation method, solid-state reaction has been extensively applied in synthesis of high photocatalytic active nanomaterial. Herein, SnO_2 and S-doped SnO_2 nanoparticles were synthesized by a facile solid-state reaction approach at low temperature using sodium dodecyl benzene sulfonate (SDBS) as a template. Paraquat was chosen as the model pharmaceutical to evaluate the photocatalytic degradation activity of the as-synthesized nanomaterial under visible light irradiation. The relationships between the photocatalytic performances and the S-doping mechanism along with the structural characteristics of the resultant photocatalysts were investigated and discussed.

1 Experimental

1.1 Chemicals and materials

Tin(Ⅳ) chloride pentahydrate ($SnCl_4\cdot5H_2O$), NaOH, sodium dodecyl benzene sulfonate ($C_{18}H_{29}NaO_3S$, SDBS), $Na_2S_2O_3\cdot5H_2O$, paraquat ($C_{12}H_{14}C_{l2}N_2$) were of analytical grade from Tianjin Kemiou Chemical Reagent Co., Ltd. China. All compounds were used as received without further purification.

1.2 Preparation of S-doped SnO_2

In a typical process, NaOH, $SnCl_4\cdot5H_2O$ and $Na_2S_2O_3\cdot5H_2O$ with a molar ratio of $n_{NaOH}:n_{SnCl_4\cdot5H_2O}:n_{Na_2S_2O_3\cdot5H_2O}=4:0.9:0.1$ and SDBS with a mass fraction of 9% of total weight were ground with a mortar for 30 min at 20 ℃ under the humidity of 75%. After stood for 4 h, the white viscous mixtures were heated at 120 ℃ for 2 h in an oven. After cooling to room temperature, the mixtures were soaked in deionized water for 6 h with stirring The obtained solid specimen were washed with distilled water thoroughly until free from Cl^- and SO_4^{2-} and dried at 105 ℃, and then were finally heated to 600 ℃ in a muffle furnace for 8 h with a heating rate of 2 ℃·min^{-1} to obtain faint yellow photocatalysts of S-doped SnO_2 ($S\text{-}SnO_{2(SDBS)}$). For comparison, white SnO_2, white $SnO_{2(SDBS)}$ and faint yellow $S\text{-}SnO_2$ were also synthesized using identical condition in the absence of SDBS as well as $Na_2S_2O_3\cdot5H_2O$, $Na_2S_2O_3\cdot5H_2O$ and SDBS, separately.

1.3 Structural and morphological characterizations

The XRD patterns were recorded by X′Pert Pro diffractometer using Cu $K\alpha$ radiation (λ=0.154 06 nm, divergence slit fixed at 0.76 mm) at a scan speed of 0.02°·min^{-1} from 5° to 80°, with a generator voltage of 40 kV, tube current of 40 mA, and a linear position sensitive detector. The surface morphologies of the synthesized photocatalysts were observed using a Field Emission Scanning Electron Microscopy (JEOL, JSM-6700F) with an accelerating voltage of 20 kV and a resolution of 1 nm. High resolution transmission electron microscopy (HRTEM) was observed with a JEOL-2100 operated at 200 kV. The FTIR spectra were investigated with a Spectrum 65 infrared spectrometer with a range of 4 000 ~400 cm^{-1} and a spectral resolution of 1 cm^{-1}. UV-Vis spectra were recorded on a Shimadzu UV-2550 spectrometer. The spectra were collected at 200~700 nm referenced to $BaSO_4$. XPS was carried out on Thermo ESCALAB250 spectrometer using monochromated Al $K\alpha$ (1 486.6 eV) source operated at 110 W. And the binding energies were referenced to the C1*s* line at 284.8 eV from adventitious carbon. The surface photovoltaic properties were performed on surface photovoltage spectrum (SPS) apparatus assembled by micro-/nanomaterials testing center of Hunan University. The surface photovoltage cell with a sandwich configuration (ITO/Sample/ITO) is shown in Fig.1. All tests were performed in indoor environment, and the data were obtained as the raw data.

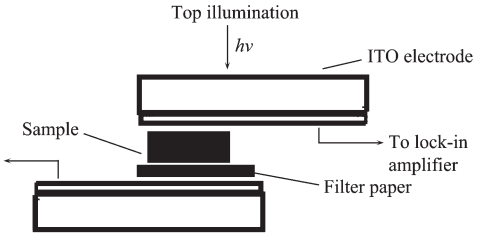

Fig.1　Setup of surface photovoltage cell configuration

1.4 Photocatalytic activity test

The photocatalytic activity of as-prepared photocatalysts was evaluated by the photocatalytic degradation of paraquat in water under visible light irradiation. Photocatalytic degradation of paraquat by the as-prepared photocatalysts was performed in a 50 mL photochemical reactor XPA-Ⅶ (Nanjing Xujiang Elechtromechanical Factory, China). A 300 W metal halogen lamp assisted with Toshiba B-47 optical filter (λ>410 nm, transmittance >90%) was used as a visible light source. The reaction solution was kept at 25 ℃± 1 ℃ by the water continuously circulated in the jacket surrounding the reactor and stirred with a magnetic stirrer throughout the experiment. Prior to illumination, a suspension of 20 mL 50 mg·L^{-1} paraquat with 20 mg photocatalyst was stirred in the dark for 60 min to achieve the adsorption-desorption equilibrium. A 5 mL solution was taken at a given time interval and centrifuged for 5 min. The concentration of paraquat was determined by UV-Vis spectrophotometer at a wavelength of 257 nm. After detection, the detection solution was taken back into the quartz tube for next use.

2 Results and discussion

2.1 Structural and morphological characterization of photocatalysts

2.1.1 XRD analysis

The wide-angle XRD patterns of the photocatalysts are displayed in Fig.2. All samples exhibit high intensity characteristic diffraction peaks of rutile SnO_2, and no any other phases appear, suggesting rutile SnO_2 is the main phase in these samples. The peaks at 2θ values of 26.5°, 33.9°, 37.9° and 52.0° are attributed to the diffraction peaks of (110), (101), (200) and (211) crystal planes of rutile SnO_2 (PDF No. 411445), respectively. From the XRD patterns, SDBS shows an increase in intensity and a decrease in the

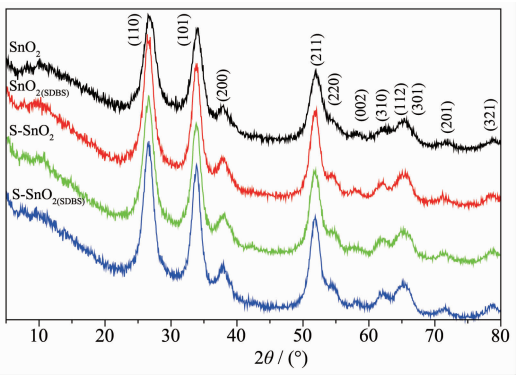

Fig.2　XRD patterns of the samples

Table 1 Data of crystallite size and crystal plane parameter for all samples

Sample	Lattice distortion constant	Crystallite size $d_{(110)}$ / nm	Crystal plane 2θ / (°)				
			(110)	(101)	(200)	(211)	(321)
SnO_2	0.318 2	4.7	26.5	34.1	38.0	51.9	78.7
$SnO_{2(SDBS)}$	0.213 2	7.0	26.4	33.9	37.7	52.1	78.0
S-SnO_2	0.264 5	5.6	26.6	33.8	38.2	51.9	78.0
S-$SnO_{2(SDBS)}$	0.242 7	6.1	26.7	33.9	38.0	51.9	78.5

peak width of diffraction peak, implying an increase in the crystallite size. Table 1 summarizes the crystallite sizes of all samples. As shown, the average crystallite sizes (d) of SnO_2, $SnO_{2(SDBS)}$, S-SnO_2 and S-$SnO_{2(SDBS)}$ particles are 4.7, 7.0, 5.6, and 6.1 nm, respectively, as calculated by Bragg′s and Scherrer′s equation (D= $0.89\lambda/(\beta\cos\theta)$) from the peak at 2θ=26.5°, suggesting that the addition of SDBS is beneficial to the growth of the SnO_2 particles and increases in crystallinity. The diffraction peaks of (110) can be seen at 26.5° and 26.6° for SnO_2 and S-SnO_2, respectively, implying that S with smaller ionic radius incorporates into the framework of SnO_2 by isomorphous substitution and subsequently leading to lattice distortion, the decrease of lattice distortion constant thus induces the increase of crystallite size. Similarly, the diffraction peaks of (110) can be observed at 26.4° and 26.7° for $SnO_{2(SDBS)}$ and S-$SnO_{2(SDBS)}$, respectively. This means that the addition of SDBS not only induces S into the lattice of SnO_2, but also could regulate the crystallite size and interplanar spacing of SnO_2 by the guiding role of the molecular structure of SDBS, inferring that these samples may possess different photoelectric properties and photocatalytic activities, which could be corroborated by the results displayed in the following experiments.

2.1.2 SEM analysis

The SEM images of SnO_2, S-SnO_2, $SnO_{2(SDBS)}$ and S-$SnO_{2(SDBS)}$ are shown in Fig.3. The SnO_2 synthesized by solid-state reaction route shows the formation of

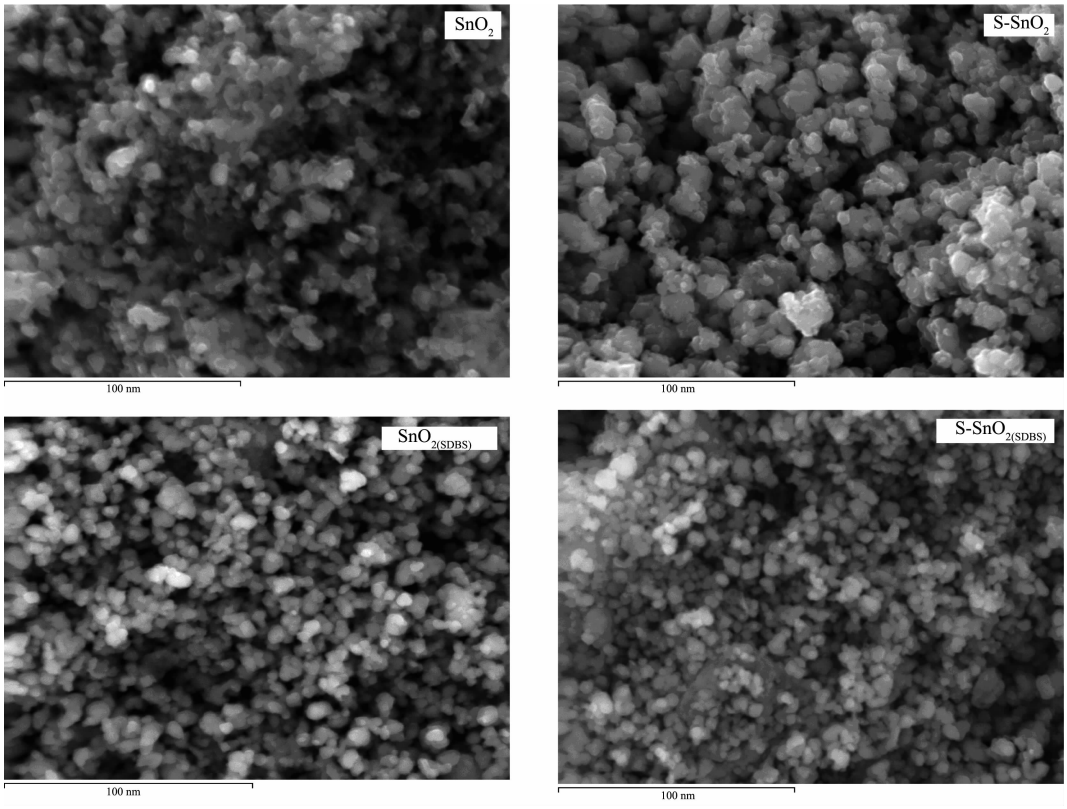

Fig.3 SEM images of samples

irregular spherical particle with a diameter distribution from 3.5~6.5 nm and an obvious agglomeration between the particles. The particulate size of S-SnO_2 is 4~7.5 nm, confirming that the reducing in particles agglomeration. It might be attributed to that $Na_2S_2O_3 \cdot 5H_2O$ hinders the diffusion and transmission of $SnCl_4 \cdot 5H_2O$ and NaOH. As expected, the particulate size range of $SnO_{2(SDBS)}$ and S-$SnO_{2(SDBS)}$ is 3.5~7.5 nm, and 3.0~8.0 nm, respectively, and the two samples show more regular sphere-like particles with smoother surfaces as compared to that of SDBS-free samples, suggesting that the addition of SDBS remarkably weakens the agglomeration of particles as its electrostatic effect and space location- obstruct effect.

The TEM images of S-$SnO_{2(SDBS)}$ particles size are shown in Fig.4. Hollow micron-sized SnO_2 spheres with a diameter of *ca.* 0.5~1 μm can be found (Fig. 4a), and these spheres are comprised of 5 nm SnO_2 nanoparticles (Fig.4b), agreeing with the crystallite size from the XRD data. The hollow micron-sized SnO_2 spheres are templated by surfactant SDBS with large hydrophilic group and long hydrophobic group, which favor the formation of spherical micelles in aqueous solutions by surfactant self-assembly, and then Sn^{4+} cations interact with SDBS anions through Coulomb forces at the interface of the spherical micelles. Subsequently, the condensation of inorganic precursors of $SnCl_4$ is improved owing to the confined growth to form SnO_2 nanoparticles and aggregate around the spherical micelles of SDBS. Finally, the surfactant SDBS template can be removed by calcination to form hollow micron-sized SnO_2 spheres and hollow spherical fragments (nanoparticles). The corresponding selected-area electron diffraction (SAED) pattern (Fig.4c) indicates that the diffraction rings can be readily assigned to the polycrystalline nature of SnO_2 phase. The corresponding high-resolution TEM (HRTEM) image (Fig.4d) shows that the interplanar distance of 0.33 nm is assigned to (110) plane of SnO_2, which means that S incorporates

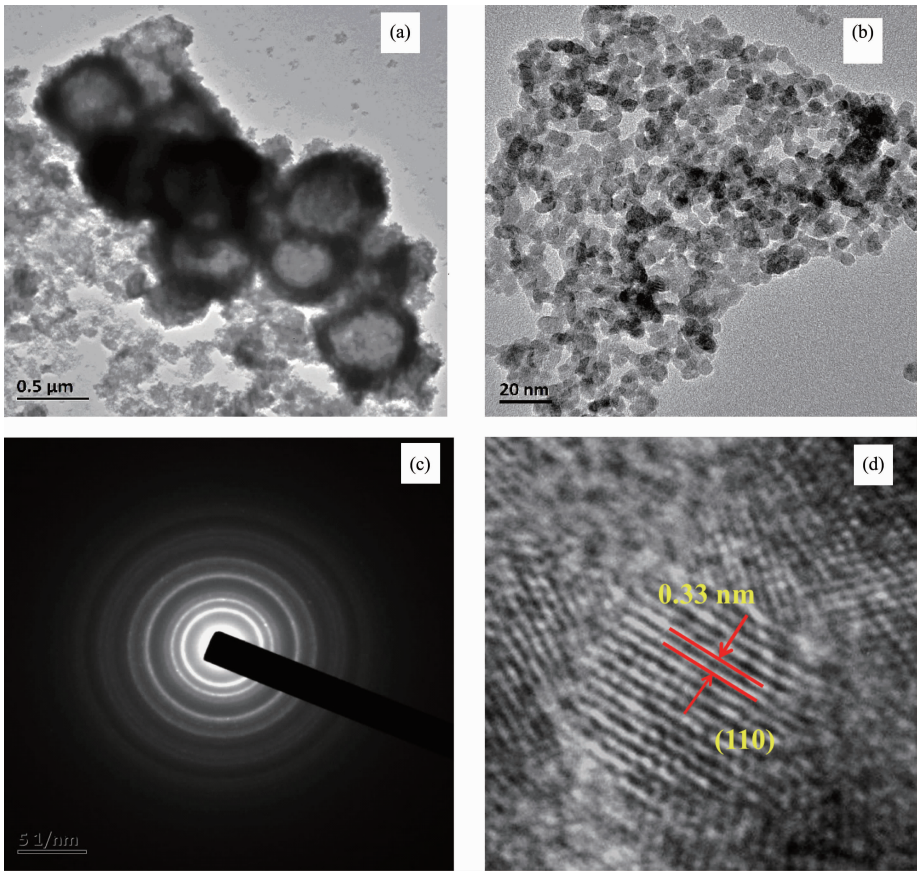

Fig.4　TEM images of S-$SnO_{2(SDBS)}$

into the lattice of SnO_2 leading to the shrink of the interplanar distance of SnO_2 compared with that of pure SnO_2 crystal (with the interplanar distance of (110) plane is 0.34 nm). The EDX elemental mapping performed on a typical hollow sphere demonstrates that the element content (atomic percentages, at%) of S within the structure is ca. 3.4%, which also suggests that a small amount of S is embedded into the lattice of SnO_2.

2.1.3 UV-Vis spectra

Fig.5 shows the UV-Vis spectra of SnO_2, S-SnO_2, $SnO_{2(SDBS)}$ and S-$SnO_{2(SDBS)}$. All samples exhibit an identical absorption in the UV region of the spectra, corresponding to the essential light absorption of SnO_2 crystal as the electron transition of SnO_2 from the valence band to the conduction band, and the UV-Vis spectra of the S-free and S-doped samples are rather similar. However, further observation reveals that the shape, slope and intensity of spectral line for the two samples are different. It may be one of evidences of the doping of S to the lattice of SnO_2. Compared with SnO_2, the absorption edge of S-SnO_2 displays a red-shift, and the corresponding band gap decrease from 3.03 to 2.93 eV extrapolated by band gap estimation formula[15]. As expected, S-$SnO_{2(SDBS)}$ also shows red-shift as compared to $SnO_{2(SDBS)}$, and the band gap is 3.14 and 3.17 eV, respectively. It can be inferred that S-doping can improve the visible light absorption of the as-prepared photocatalysts due to the embedding of S into the SnO_2 lattice. Furthermore, the slower rate of diffusion and mass transfer in the solid-state reaction result in the crystal structure defects and

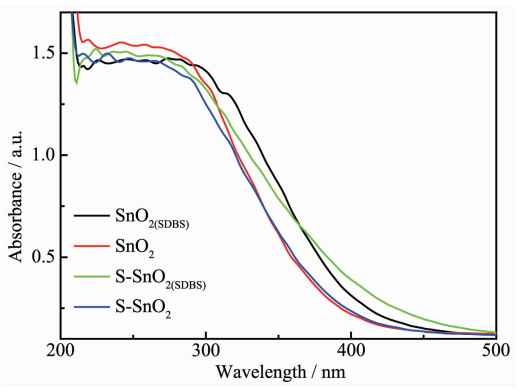

Fig.5 UV-Vis spectra of the samples

imperfections, leading to the reduction of crystallinity and narrowing of the band gap of SnO_2[16-18].

2.1.4 FTIR spectra

The FTIR spectra are shown in Fig.6. The absorbing peaks in the range of 620~640 cm^{-1} can be assigned to the stretching vibration modes and bending vibration of Sn-O bond in SnO_2[19-20]. By comparing with the SnO_2 and $SnO_{2(SDBS)}$, it can be found that the samples of S-SnO_2 and S-$SnO_{2(SDBS)}$ exhibit absorbing peaks at 1 151 and 978 cm^{-1}, and 1 130 and 931 cm^{-1}, respectively, which can be attributed to the asymmetrical stretching vibration of O-S and bending vibration of Sn-O-S in S-doped SnO_2[13,21]. Moreover, the broad characteristic bands centered at 3 368, 3 185, 3 412 and 3 400 cm^{-1} for SnO_2, S-SnO_2, $SnO_{2(SDBS)}$, and S-$SnO_{2(SDBS)}$, respectively, can be assigned to the stretching vibration mode of H-O. It can be inferred from the difference of the peak position of H-O that the surficial polarities of resultant photocatalysts are different as the different degrees of association of H-O. The peaks at 1 630 cm^{-1} are attributable to the bending vibration of H-O. Meanwhile, it is also found that the doping of S changes the peak position of bending vibration of H-O[16].

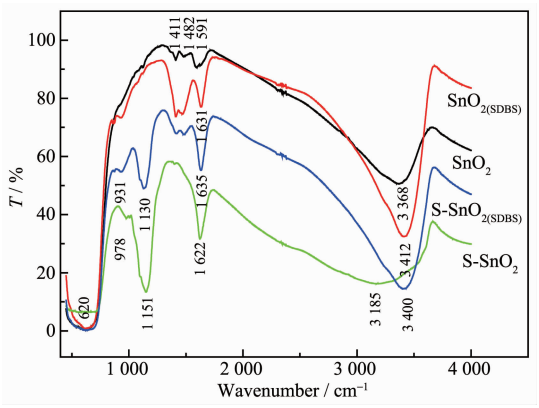

Fig.6 FTIR spectra of the samples

2.1.5 XPS analysis

The chemical compositions and chemical states of S-doped SnO_2 were characterized by XPS (Fig.7 and 8). The surface survey spectrum (Fig.7) shows the presence of the Sn4*d*, Sn4*s*, S2*p*, O1*s*, C1*s*, Sn3*d* and Sn3*p* peaks in the samples. The presence of C peak is due to the adventitious hydrocarbon from XPS instrument itself and the residual organic groups from

the SDBS. The high-resolution XPS spectra of the Sn, O and S elements are provided in Fig.8. For S-$SnO_{2(SDBS)}$, two peaks for the Sn3$d_{5/2}$ and Sn3$d_{3/2}$ observed at 485.1 and 494.7 eV, respectively, are both assigned to Sn^{4+} in rutile phase of SnO_2[22]. The spectrum of S2*p* shows a broad asymmetric curve at 168.0 eV, which can be deconvoluted into two peaks with binding energies at 167.6 eV for S(Ⅳ) and 169.5 eV for S(Ⅵ)[22], respectively, with a S(Ⅳ)/S(Ⅵ) molar ratio of 0.9. The binding energy peaks for O1*s* observed at 529.2 and 531.0 eV are originated from Sn-O-Sn bond in SnO_2 and the adsorbed oxygen, respectively. For S-SnO_2, the peaks of Sn3*d* shift slightly to lower binding energies compared with that of S-$SnO_{2(SDBS)}$. The peaks positions of S2*p* are identical with S-$SnO_{2(SDBS)}$. Comparatively, S(Ⅳ)/S(Ⅵ) molar ratio of S-SnO_2 is 1.43, indicating S(Ⅳ) is significantly more than S(Ⅵ), implying that the addition of SDBS remarkably influences the valence states of S, which means that these two samples may possess different photocatalytic performance. Combined with the XRD results, the characteristic diffraction peaks of SnO_2 for pure SnO_2 and S-doped SnO_2 does not exhibit any shifts except a change in the full width at half-maximum, implying no variation in the lattice parameters but lattice distortion appears as S(Ⅳ) and S(Ⅵ) are embedded into the lattice of SnO_2 to form $Sn_{1-x}S_xO_2$[23]. Since S is doped as S(Ⅳ)/S(Ⅵ), the state of mixing 3*p* of S with 2*p* of O should be clear, they should mainly contribute to the conduction band in S-doped SnO_2. That is, the S-O-Sn bond on the nanomaterial surface must be presented in FTIR spectra. Usually, if the S is doped as S^{2-}, such kind of orbital mixing should occur, but not for the S doped as S(Ⅳ)/S(Ⅵ) oxidation state. These are consistent with the results in Fig.3 and Fig.4. Therefore, the origin of the slight extension of the visible light absorption after S doping is undoubted. It might be due to the nanoparticle size, defect effect, and mixing of p orbitals of S(Ⅳ)/S(Ⅵ) with O^{2-}.

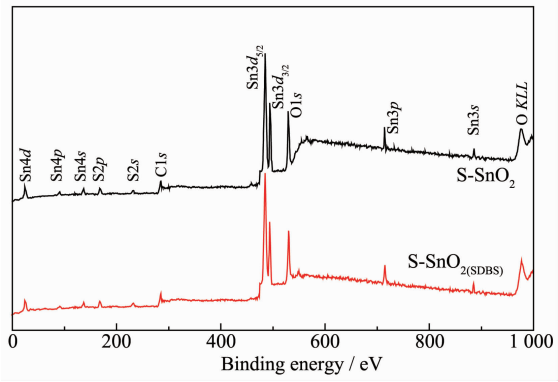

Fig.7　Surface survey XPS spectra of S-doped SnO_2

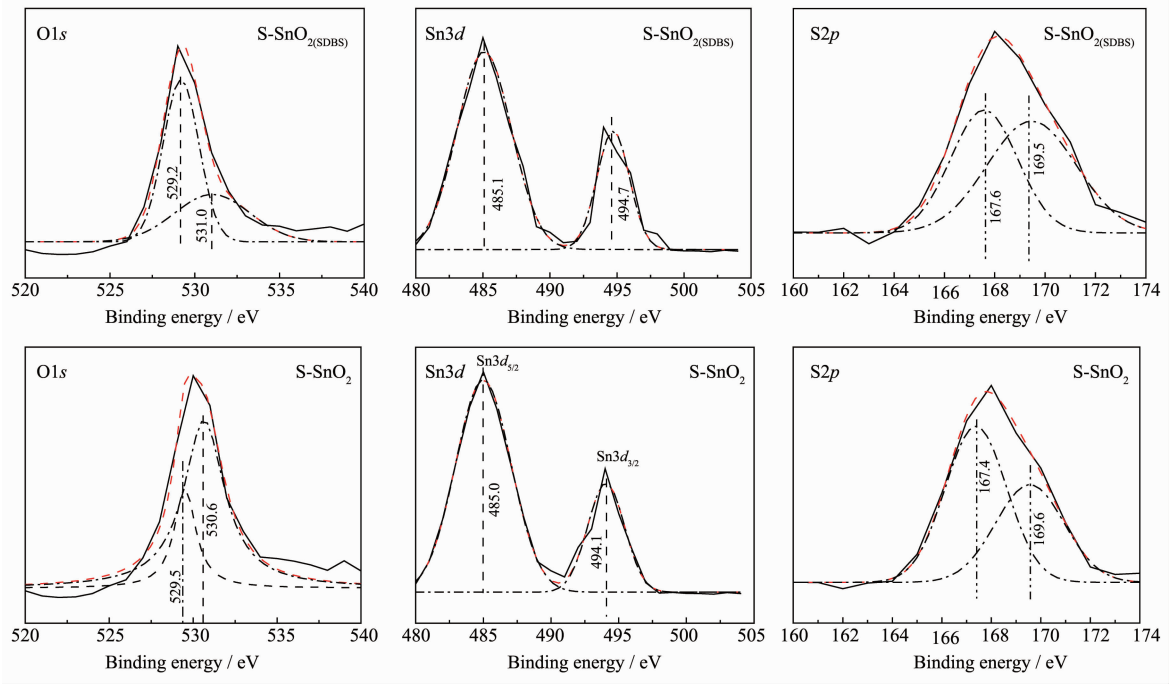

Fig.8　High-resolution XPS spectra of O1*s*, Sn3*d* and S2*p* for S-SnO_2 and S-$SnO_{2(SDBS)}$

2.2 Photocatalytic degradation of paraquat

The photocatalytic degradation of a typical herbicide, paraquat under visible light irradiation is shown in Fig.9. These samples show obviously different adsorption capabilities towards paraquat (c_0=50 mg·L^{-1}) due to the different surface states, and the adsorption equilibrium is achieved within 60 min for all samples. No noticeable changes of paraquat concentration could be observed within 120 min under visible light irradiation without the addition of photocatalyst, indicating that only photolysis could not efficiently decompose the paraquat. As expected, the S-doped SnO_2 exhibits high photocatalytic activity, and it follows an order of SnO_2(6.5%)<S-SnO_2(33.3%)<$SnO_{2(SDBS)}$ (74.8%)<S-$SnO_{2(SDBS)}$ (95.2%), implying that S-$SnO_{2(SDBS)}$ could produce more photogenerated charges and thereby possesses higher photocatalytic degradation activity under visible-light irradiation, which could degrade paraquat of 95% into the 4-carboxyl-1-methylamine production[24] within 2 h.

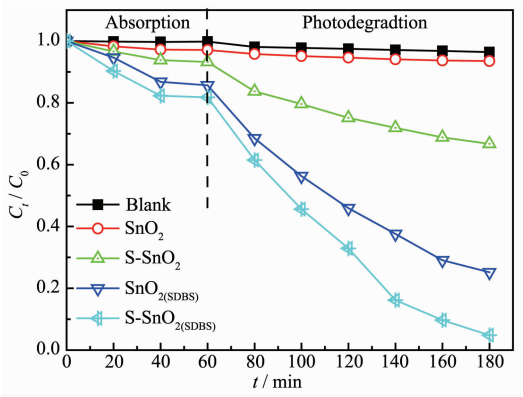

Fig.9 Photodegradation of paraquat under visible light irradiation

2.3 Photoeletrochemical characterization

Fig.10 shows the surface photovoltaic spectra (SPS) of samples with applied potential bias of +0.5 V. Among all investigated samples, the surface photovoltage response of these nanopowder is positively correlated to the UV absorption intensity and range, that is, the surface photovoltage follows the order of S-$SnO_{2(SDBS)}$ (0.006 36 mV)>$SnO_{2(SDBS)}$ (0.005 01 mV) > S-SnO_2 (0.002 22 mV) > SnO_2 (0.000 46 mV). Comparatively, the surface photovoltage of S-$SnO_{2(SDBS)}$ is 13.8 times higher than that of SnO_2 under the same condition, suggesting that S-doped SnO_2 have higher efficiency to transport the photogenerated electrons than SnO_2. From Fig.8, the surface photovoltage response of the samples can also be observed at 420~600 nm with a weak peak, attributing to the existence of a large amount of surfaces states and Dember effect. The surface state could change the configuration of nanoparticle′s surface atoms, electron spin and electronic transition. Based on EFISPS principle, the surface state is sensitive towards the external electric field, an external electric field enhances the transition probability of surface state to generate surface photovoltage response signals in the long wavelength [25]. The stronger of the SPS signal is, the higher the efficiency of photoinduced charge separation. This is consistent with the results of visible-light degradation. Simultaneously, surface oxygen vacancies and defects enhance the separation of photogenerated charges at the interface, resulting in the higher photodegradation efficiency of paraquat.

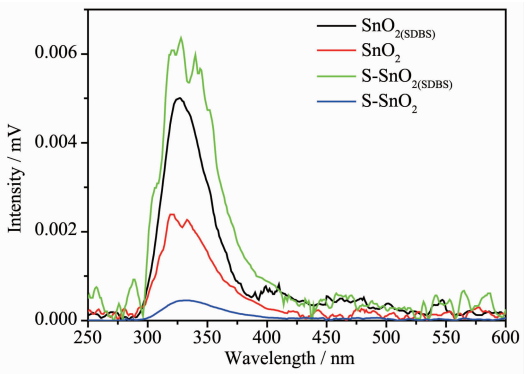

Fig.10 Electrical field induced surface photovoltage spectra in the samples

From the results above, it can be deduced that the surficial states of photocatalyst have a significant effect on the photocatalytic activity. As for S-$SnO_{2(SDBS)}$, the S element is successfully incorporated into the lattice of SnO_2 with S(Ⅳ)/S(Ⅵ) by substituting Sn^{4+}, rather than embedded into the interstice of SnO_2 lattice, thereby leading to lattice distortion. The S3*p* level could mix with O2*p* which results in the narrowing of the band gap and enhancing the photocatalytic activity. Moreover, the formation of the localized midgap state above the top of the valence band for SnO_2 might be responsible for increasing the

photoactivity of SnO_2 in the visible region[26]. The average size of S-$SnO_{2(SDBS)}$ is lower than 6 nm as the doping of S, leading to the enhanced absorption of light because of the quantum size effect and subsequently enhancing the amount of photo-induced carrier. Additionally, a large amount of hydroxyl groups in S-$SnO_{2(SDBS)}$ are beneficial to generating highly reactive ·OH, thus accelerating the degradation of paraquat. It should also be noted that the ratio of S(Ⅵ) in S-$SnO_{2(SDBS)}$ is obviously more than that of S-SnO_2, which also enhances the degradation of paraquat because S(Ⅵ) has stronger oxidation capacity than S(Ⅳ).

3 Conclusions

In this work, S-doped SnO_2 nanoparticles with superior visible light photocatalytic activity was fabricated via a facile solid state synthesis approach at low temperature using sodium dodecyl benzene sulfonate (SDBS) as template. The S element is successfully incorporated into the lattice of SnO_2 with S(Ⅳ)/S(Ⅵ) instead of embedding into the interstice of SnO_2 lattice. S-doped SnO_2 could significantly improve visible light utilization property, thus resulting in narrowed band gap. SDBS has a significant regulating effect on the surficial structure of photocatalysts. The photocatalytic activity shows significant correlation with particle size, particle size distribution and the ratio of S(Ⅳ)/S(Ⅵ). S-doped SnO_2 exhibits higher photocatalytic activity, and it follows an order of SnO_2<S-SnO_2<$SnO_{2(SDBS)}$<S-$SnO_{2(SDBS)}$, in which S-$SnO_{2(SDBS)}$ could degrade 95.4% paraquat within 2 h.

Acknowledgements: This work was supported by the Education Quality Promotion Foundation of Department of Education, Guizhou Province, China (No.[2011]278-01), Guizhou Province Characteristic Leading Academic Discipline Project in Material Physics and Chemistry (No.[2011]208), Characteristic Key Laboratory Construction Fund of Guizhou Province (No.[2012]014), and Science and Technology Innovation Talent Team Foundation of Guizhou Province, China (No.[2013]4029).

References:

[1] SU Shao-Quan(苏少泉), GENG He-Li(耿贺利). *Pesticide*(农药), **2008**,**47**(4):244-247

[2] WANG Zhai-Yu(王载宇). *J. Medical Frontier*(医药前沿), **2011**,**1**(12):61-62

[3] JIAO Jian(焦剑), SONG Ji-Mei(宋继梅), ZHANG Xiao-Xia(张小霞), et al. *Guangzhou Chemical Industry*(广州化工), **2010**,**8**(3):138-141

[4] ZHENG Wen(郑文), TANG Wen-Hao(唐文浩). *Anhui Agricultural Sciences*(安徽农业科学), **2007**,**35**(8):2370-2371

[5] LIU Chun-Ming(刘春明), FANG Li-Mei(方丽梅), ZU Xiao-Tao(祖小涛). *Acta Phys. Sin.*(物理学报), **2009**,**58**(2):936-940

[6] Emons T T, Li J, Nazar L F. *J. Am. Chem. Soc.*, **2002**,**124**(29):8516-8517

[7] Monredon S, Cellot A, Delattre L, et al. *J. Mater. Chem.*, **2002**,**12**:2396-2400

[8] Rockenberger J, Zum F U, Tischer M, et al. *J. Chem. Phys.*, **2000**,**112**(9):4296-4304

[9] LU Yao(逯瑶), WANG Pei-Ji(王培吉), ZHANG Chang-Wen(张昌文), et al. *Acta Phys. Sin.*(物理学报), **2011**,**60**(6):223-229

[10]LU Yao(逯瑶), WANG Pei-Ji(王培吉), ZHANG Chang-Wen(张昌文), et al. *Acta Phys. Sin.*(物理学报), **2012**,**61**(2):23101-23106

[11]CHI Jun-Hong(池俊红), WANG Juan(王娟). *Acta Phys. Chim. Sin.*(物理化学学报), **2010**,**26**(8):2306- 2310

[12]OUYANG Pan(欧阳攀), ZHANG Hong(张鸿), LI Gen(李根), et al. *Electronic Components and Materials*(电子元器件及材料), **2012**,**6**(31):10-14

[13]XU Ke-Jing(许珂敬), SHANG Chao-Feng(尚超峰), LI Fang(李芳). *Chinese J. Nonferrous Metals*(中国有色金属学报), **2008**,**18**(5):884-889

[14]ZHOU Wu-Yi(周武艺), CAO Qing-Yun(曹庆云), TANG Shao-Qiu(唐绍裘), et al. *J. Inorganic Materials*(无机材料学报), **2006**,**21**(4):776-782

[15]LIU Shou-Xin(刘守新), LIU Hong(刘鸿). *Foundation and Application of Photocatalysis and Photoelectro-Catalysis*(光催化及与光电催化基础与应用). Beijing: Beijing Chemical Industry Press, **2005**:135

[16]CHANG Jian-Hua(常建华), DONG Qi-Gong(董绮功). *Principle and Analysis of Spectrum*(波谱原理与解析). Beijing: Beijing Science Press, **2006**:84

[17]ZHANG Yi-Hua(张义华), ZHANG Jing-Xin(张景新), WANG Xue-Qing(王学勤), et al. *J. Dalian University of Technology*(大连理工大学学报), **2000**,**40**(1):64-66

[18]Wark M, Ekloff G S, Jaeger N I. *Stud. Surf. Sci. Catal.*, **1991**, **69**:189-197

[19]Adans D M. *Metal-Ligand and Related Vibrations*. London: Edward Arnold, **1967**.

[20]Socrates G. *Infrared Characteristic Group Freqencies*. New York: Wiley, **1980**.

[21]Randeniya L K, Murphy A B, Plumb I C. *J. Mater. Sci.*, **2008**,**43**:1389-1399

[22]Themlin J M, Chtaib M, Henrard L, et al. *Phys. Rev. B*, **1992**, **46**(4):2460-2466

[23]Satish C B M, Samuel J T, Glenn A, et al. *Geochim. Cosmochim. Acta*, **1998**,**62**(21/22):3499-3514

[24]Slade P. *Nature*, **1965**,**207**:515-516

[25]XUE Yong-Qiang(薛永强). *Thesis for The Doctorate of Taiyuan University of Technology*(太原理工大学博士学位论文), **2005**.

[26]Daghrir R, Drogui P, Robert D. *Ind. Eng. Chem. Res.*, **2013**, **52**:3581-3599